Elliptical vibration chiseling: a novel process for texturing ultra-high-aspect-ratio microstructures on the metallic surface

To cite this article before publication: Zhiwei Li *et al* 2024 *Int. J. Extrem. Manuf.* in press https://doi.org/10.1088/2631-7990/ad1bbb

Elliptical vibration chiseling: a novel process for texturing ultra-high-aspect-ratio microstructures on the metallic surface

Journal:	*International Journal of Extreme Manufacturing*
Manuscript ID	IJEM-111119.R2
Manuscript Type:	Paper
Keywords:	Metallic microstructure, High aspect ratio, Backward-moving cutting, Vibration cutting, Chiseling, Material deformation

Elliptical vibration chiseling: a novel process for texturing ultra-high-aspect-ratio microstructures on the metallic surface

Zhiwei Li[1, 2], Jianfu Zhang[1, 2], Zhongpeng Zheng[1, 2], Pingfa Feng[1, 2, 3], Dingwen Yu[1, 2], Jianjian Wang[1, 2, *]

1. State Key Laboratory of Tribology in Advanced Equipment, Department of Mechanical Engineering, Tsinghua University, Beijing 100084, China
2. Beijing Key Laboratory of Precision/Ultra-precision Manufacturing Equipments and Control, Department of Mechanical Engineering, Tsinghua University, Beijing 100084, China
3. Division of Advanced Manufacturing, Shenzhen International Graduate School, Tsinghua University, Shenzhen 518055, China

*Corresponding authors. E-mails: wangjjthu@tsinghua.edu.cn

Abstract

High-aspect-ratio metallic surface microstructures are increasingly demanded in breakthrough applications, such as high-performance heat transfer enhancement and surface plasmon devices. However, the fast and cost-effective fabrication of high-aspect-ratio microstructures on metallic surfaces remains challenging for existing techniques. This study proposes a novel cutting-based process, namely elliptical vibration chiseling (EV-chiseling), for the high-efficiency texturing of surface microstructures with an ultrahigh aspect ratio. Unlike conventional cutting, EV-chiseling superimposes a microscale elliptical vibration on a backward-moving tool. The tool chisels into the material in each vibration cycle to generate an upright chip with a high aspect ratio through material deformation. Thanks to the tool's backward movement, the chip is left on the material surface to form a microstructure rather than falling off. Since one microstructure is generated in one vibration cycle, the process can be highly efficient using ultrafast (>1 kHz) tool vibration. A finite element analysis model is established to explore the process mechanics of EV-chiseling. Next, a mechanistic model of the microstructured surface generation is developed to describe the microstructures' aspect ratio dependency on the process parameters. Then, surface texturing tests are performed on copper to verify the efficacy of EV-chiseling. Uniformed micro ribs with a spacing of 1~10 μm and an aspect ratio of 2~5 have been successfully textured on copper. Compared with the conventional EV-cutting that uses a forward-moving tool, EV-chiseling can improve the aspect ratio of textured microstructure by up to 40 times. The experimental results also verify the accuracy of the developed surface generation model of microstructures. Finally, the effects of elliptical trajectory, depth of cut (DoC), tool shape, and tool edge radius on the surface generation of micro ribs have been discussed.

Keywords: metallic microstructure; high aspect ratio; backward-moving cutting; vibration cutting; chiseling; material deformation.

1. Introduction

Metallic surface microstructures are attracting increasing attention in many industrial fields, such as optics[1], heat transfer[2], biology[3], and tribology[4], due to their superior performance in enhancing surface properties or enabling new functionalities[5]. The aspect ratio, height to width, is a critical geometric parameter of metallic microstructures that significantly affects their performance. Increasing the aspect ratio could benefit the applications. For example, the high-aspect-ratio surface microstructures on pure copper could improve the corrosion resistance of the raw material by 18.5% [6]. Besides, the high-aspect-ratio microchannels could increase the heat transfer indexes of the surface, including the critical heat flux and the heat transfer coefficient [7]. The high-efficiency and cost-effective fabrication of high-aspect-ratio metallic microstructures is vital to ensure applications.

The fabrication method of high-aspect-ratio metallic microstructures can be classified as nonmechanical and mechanical. The representative nonmechanical methods include lithography[8], femtosecond laser texturing[9], 3D metallic printing[10], micro-electric discharge machining (Micro-EDM)[11], chemical etching, electroforming, and nanoimprints. Lithography is the most commonly used technique for creating high-aspect-ratio microstructures. However, it mainly aims at silica-based materials and polymers[12, 13]. It is toilsome and expensive for lithography to texture large-scale metallic surfaces due to the high equipment cost and multistep process procedure. Femtosecond laser texturing can fabricate microstructures on various metallic materials [14-16]. However, high efficiency and aspect ratio cannot be simultaneously achieved for femtosecond laser texturing[17, 18]. 3D printing can develop metallic microstructures with arbitrary geometries and exhibits superior performance in the flexible patterning capability[19]. However, the efficiency of 3D metallic printing is too low for large-area fabrication. Micro-EDM is good at fabricating complex 3D microstructures with high aspect ratios, but the low achievable scale and efficiency for generating patterned microstructures block its application in the industry[20].

Chemical etching, electroforming, and nanoimprints are also classical nonmechanical methods for the fabrication of high-aspect-ratio microstructures. Chemical etching can generate high-aspect-ratio structures such as nanosheets, which can be applied in electrochemical water splitting[21] like hydrogen evolution reaction[22] and electrocatalysis[23]. However, chemical etching is more adept at creating nanoscale structures than microscale structures. Electroforming is theoretically possible to generate metallic microstructures with a limitless aspect ratio[24] on a submillimeter scale [25-27], but its dependence on a mask mold remains challenging to manufacture, restricting its process flexibility. Nanoimprints can generate ultra-thin metallic nanostructures with a high aspect ratio and could be used as transparent electrodes for organic solar cells[28-30]. However, nanoimprint is a multi-step process that relies on the use of mask mold, making it suffer from low process stability and flexibility.

The mechanical methods are the other widely adopted technique group for metallic surface texturing with the advantages of high flexibility and low cost, represented by tool servo cutting[31], micromilling[32, 33], fly cutting[34], grinding[35], and vibration-assisted cutting[36]. Tool servo cutting with a single crystal diamond tool could fabricate optical metallic microstructures like micro lens arrays with high accuracy and quality[37], but it has the drawbacks of low efficiency and small scale. Micormilling can fabricate various metallic microstructures, including dimples, grooves, and riblets[38]. However, the tool diameter limits the achievable structure size by micromilling[39]. Fly cutting can ensure surface quality uniformity and provide flexibility for machining hierarchical microstructures[40], but it is challenging to generate high-aspect-ratio microstructures. Grinding is fit for fabricating microstructures like micropillars and grooves on difficult-to-cut materials[41]. However, the achievable aspect ratio is not high due to the size limitation of the grinding tool.

Besides, vibration-assisted cutting[42], especially elliptical vibration cutting (EV-cutting)[43, 44], has emerged as a promising surface texturing approach for metallic materials. In vibration-assisted cutting, a microscale vibration is superimposed into the tool by a nonresonant[45, 46] or resonant[47] device. Tool vibration traces are left on the material surface to form microstructures[48, 49], whose shape is a function of the tool geometry and trajectory[50]. So, vibration-assisted cutting has high control precision of structural geometry[46, 51], and high process flexibility. Moreover, vibration-assisted cutting can be very efficient for large-area microstructure texturing with a texturing rate of as high as 20 000·s^{-1} if an ultrasonic tool vibration is adopted. Currently, the surface texturing principle based on vibration-assisted cutting has been realized in turning[52], milling[53], planning[54], and so on. In addition to single-scale structures like dimples[55, 56] and grooves[57], vibration-assisted cutting can also fabricate hierarchical microstructures like multiscale microchannels[58] and multiscale dimples[59], which have improved performance in applications such as heat transfer[60], anti-fouling[61], and cell bioactivity[62]. However, the aspect ratio of microstructures created by vibration-assisted cutting is still very limited (far less than 1).

In summary, it remains challenging to fabricate high-aspect-ratio microstructures on large-area metallic surfaces with high efficiency, low cost, and high flexibility. Though the cutting-based texturing method has the advantages of high efficiency, low cost, and high flexibility and capacity to texture large-area surfaces, its achievable aspect ratio of microstructure is restricted. This study proposes a novel cutting-based process, namely elliptical vibration chiseling (EV-chiseling), for the fabrication of ultra-high-aspect-ratio microstructures, simultaneously inheriting the advantages of the cutting-based texturing principle. First, the process mechanics in EV-chiseling is illustrated by FEA. Then, a mechanistic model is developed to establish the effects of process parameters on the geometries of microstructures. Finally, machining tests with different vibration trajectories, depth-of-cut (DoC), and tools are conducted to verify the efficacy of the proposed EV-chiseling.

2. Principle of elliptical vibration chiseling

2.1 Illustration of elliptical vibration chiseling

The process principle of EV-chiseling is demonstrated in **Figure 1**. In EV-chiseling, an elliptical vibration trajectory is added to the tool, which moves backward in contrast to conventional cutting[63] and EV-cutting[36, 49, 50]. The tool chisels into the material in each vibration cycle to generate an upright chip with a high aspect ratio through material deformation. Owing to the tool's unique backward movement, the chip is left on the material surface to form a ribbed microstructure rather than falling off. The height of the chiseled microstructure is larger than the width. In contrast, the aspect ratio of the created microstructures by EV-cutting is small, whose height is much smaller than the width. To ensure the process efficacy, the process parameters of EV-chiseling should match each other, including the tool shape, the elliptical trajectory (defined by semimajor axis a, seminar axis b, and inclination angle θ), the vibration frequency f, the DoC, and the nominal cutting velocity V_c. The vibration frequency determines the generation rate of microstructure in EV-chiseling, so the machining efficiency of EV-chiseling can be very high if ultrafast tool vibration can be adopted. EV-chiseling exhibits excellent potential for fast fabricating high-aspect-ratio microstructures on metallic surfaces outperforming existing methods.

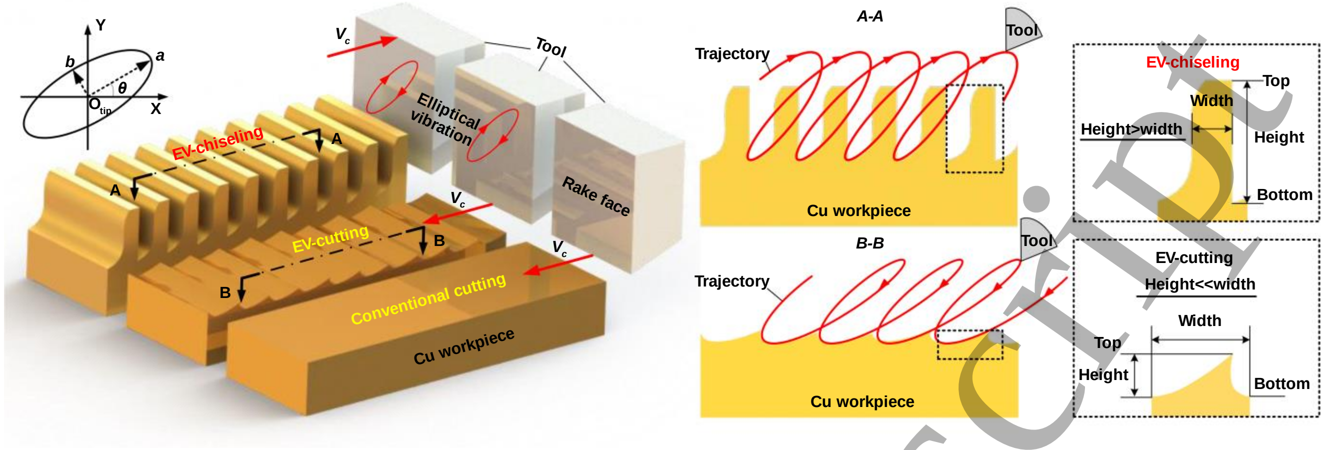

Figure 1. The process principle of EV-chiseling, EV-cutting, and conventional cutting methods. *A-A* and *B-B* refer to the section view of EV-chiseling and EV-cutting, respectively.

In order to successfully perform the EV-chiseling, knowledge gaps such as the underlying mechanism governing the control of process parameters on the structure formation and what kind of vibration trajectory is suitable should be filled. Moreover, technological bottlenecks regarding the design of high-performance vibration device should be addressed. The vibration device is demanded to be able to generate a high-frequency, large-amplitude, and controllable vibration trajectory for guaranteeing the performance of EV-chiseling in efficiency, flexibility, and quality.

2.2 Finite element analysis of microstructure generation

Finite element analysis (FEA) is performed to explore the process mechanics in EV-chiseling. A 2D FEA model is constructed using Abaqus. The geometric model (100 μm×30 μm) of the workpiece and boundary conditions for FEA is shown in **Figure 2**. The tool is set as a rigid body with a clearance angle of 10°, a rake angle of 0°. The Johnson-Cook constitutive model is used to describe the mechanical behavior of the workpiece material in the EV-chiseling, as expressed below:

$$\sigma = (A + B\varepsilon_p^n)\left(1 + C\ln\frac{\dot{\varepsilon}}{\dot{\varepsilon}_0}\right)\left[1 - \left(\frac{T - T_r}{T_m - T_r}\right)^m\right] \quad (1)$$

where A, B, C, n, and m are the typical material constants of the Johnson-Cook constitutive equation. σ is the Von Mises equivalent flow stress, ε_p is the equivalent plastic strain, $\dot{\varepsilon}$ is the plastic strain rate, $\dot{\varepsilon}_0$ is the reference plastic strain rate of material. T, T_r, and T_m are the deformation, reference, and melting temperatures, respectively. Besides, the damage evolution of material in the FEA is modeled by Johnson-Cook cumulative damage law, expressed as:

$$\bar{\varepsilon}_{JC} = \left[D_1 + D_2 e^{D_3\frac{p}{\bar{\varepsilon}}}\right]\left[1 + D_4\ln\left(\frac{\dot{\varepsilon}}{\dot{\varepsilon}_0}\right)\right]\left(1 + D_5\left(\frac{T - T_r}{T_m - T_r}\right)\right) \quad (2)$$

where the ratio of $p/\bar{\sigma}$ is defined as the stress triaxiality, D_1~D_5 are five constants determined by experiments. The mechanical properties, the Johnson-Cook constitutive parameters, and five constants of the copper material are listed in **Table 1**[64, 65].

Table 1. Mechanical properties, Johnson-Cook constitutive parameters, and five constants of copper.

Density/ (kg m^{-3})	Elastic Modulus/ GPa	Poisson's Ratio	Thermal conductivity/ (W m^{-1} K^{-1})	Specific heat/ (J kg^{-1} K^{-1})	*A*/ MPa	*B* /MPa	*n*	*C*	*m*	D_1	D_2	D_3	D_4	D_5
8 940	100	0.31	386	383	99.7	263	0.23	0.029	0.98	-0.068	0.451	-0.952	0.036	0.697

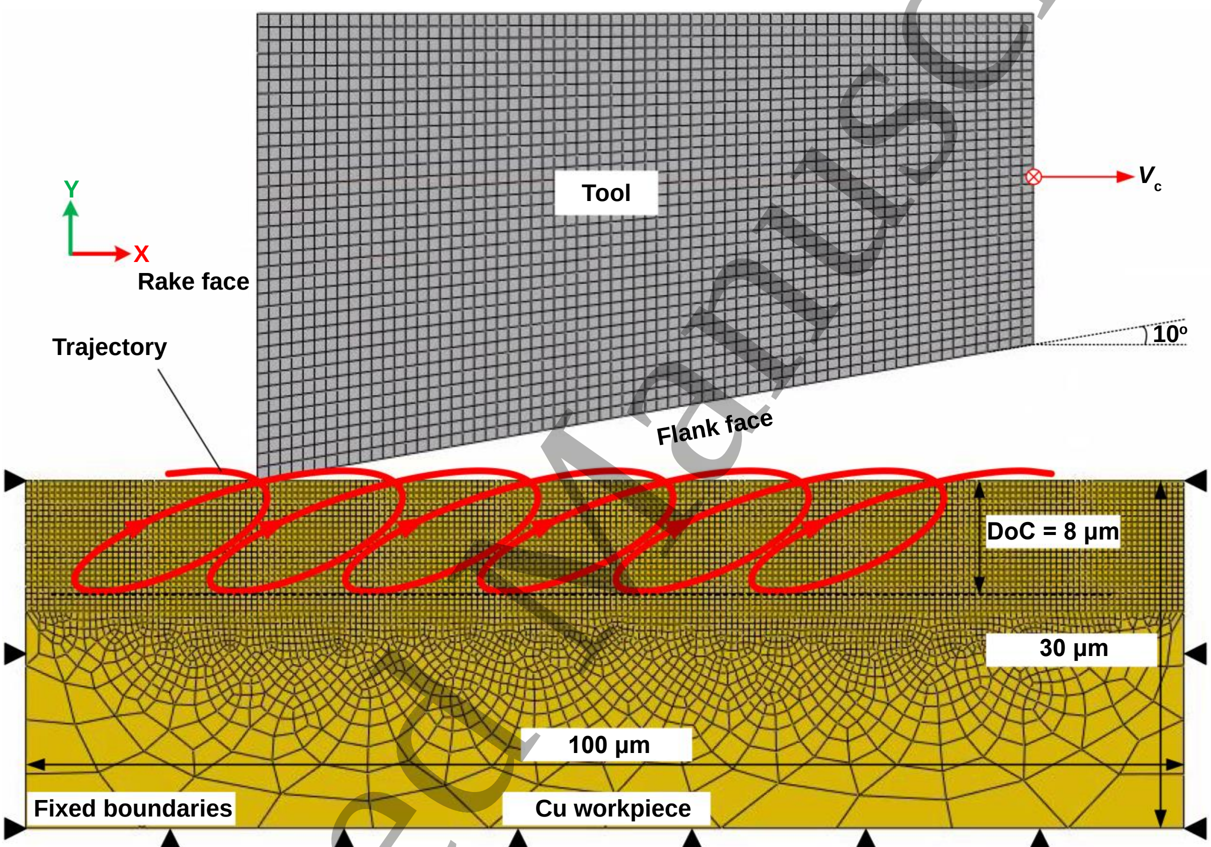

Figure 2. FEA setups of EV-chiseling.

In FEA, the nominal cutting velocity V_c is set as 10 mm·s^{-1}, the DoC is 8 μm, and the vibration frequency f is 1 000 Hz. For an inclined elliptical tool trajectory (a = 10 μm, b = 3 μm, and θ = 20°). The instantaneous tool velocities are defined as,

$$\begin{cases} v_x = A_x\cos(-2\pi ft) + B_x\sin(-2\pi ft) + V_c \\ v_y = A_y\cos(-2\pi ft) + B_y\sin(-2\pi ft) \end{cases} \quad (3)$$

where t is time, v_x and v_y are the instantaneous tool velocities in the cutting and DoC directions. A_x and A_y are the velocity constants of sines, B_x and B_y are the velocity constants of cosines of x and y axes. The velocity constants could be expressed as:

$$\begin{cases} A_x = -2\pi\, fb\sin\theta \\ A_y = 2\pi\, fb\cos\theta \\ B_x = -2\pi\, fa\cos\theta \\ B_y = -2\pi\, fa\sin\theta \end{cases} \tag{4}$$

The FEA results of the variation of stresses during EV-chiseling are demonstrated in **Figure 3**. The EV-chiseling process in each vibration cycle can be divided by five points P_1, P_1', P_2, P_3, and P_4 of the trajectory into four steps: Move-in, Cut-in, Deforming, and Move-out. P_1 and P_1' are the upside points for two adjacent tool trajectories. P_2 is where the tool starts to contact the workpiece. P_3 and P_4 are the lowest and leftmost points of the tool trajectory, respectively.

In the Move-in step (**Figure 3**(a)), the tool moves toward the workpiece following the tool path from point P_1 to P_2, and no material is cut by the tool. **In the Cut-in step** (**Figure 3**(b)), the tool cuts into the workpiece material following the tool path from point P_2 to P_3. With the gradual increases of instantaneous DOC, two kinds of tool-workpiece interaction occur. One is the chip formation on the tool rake face, where the volume of material can be assumed as unchanged. While the other is the material extrusion on the tool flank face, where the volume of material is reduced. **In the Deforming step** (**Figure 3**(c)), the tool moves from point P_3 to P_4. The material continues to deform to form a higher chip, which can be regarded as a high-aspect-ratio microstructure. The horizontal distance of P_3 and P_4, denoted as overcut distance, is a critical factor affecting microstructure generation. If the overcut distance exceeds the microstructure spacing V_c/f, the chip can be fractured and fall off the workpiece surface. So, to guarantee the efficacy of EV-chiseling, the following condition should be satisfied,

$$\left| x_{P_3} - x_{P_4} \right| \leq \frac{V_c}{f} \tag{5}$$

In the Move-out step (**Figure 3**(d)), the tool leaves the workpiece surface following the tool path from point P_4 to P_1' to prepare for the next cutting cycle. The material deformation rule obtained by FEA for the EV-chiseling provides a fundamental basis for subsequent analytical modeling of microstructures' geometries. Due to the extrusion-dominated chip formation in this new process, the influence of residual stress on the microstructure is considered. The simulated residual stress σ of microstructures is calculated and shown in **Figure 3**(e). The maximum tensile stress is about 74.9 MPa, the maximum compress stress is about 127.5 MPa, while the average σ is about -23.8 MPa (compress stress). Therefore, the overall residual stress is acceptable. The maximum tensile stress is far less than the ultimate tensile strength of copper materials (about 300 MPa), thus, the microstructure obtained by EV-chiseling can keep a good strength.

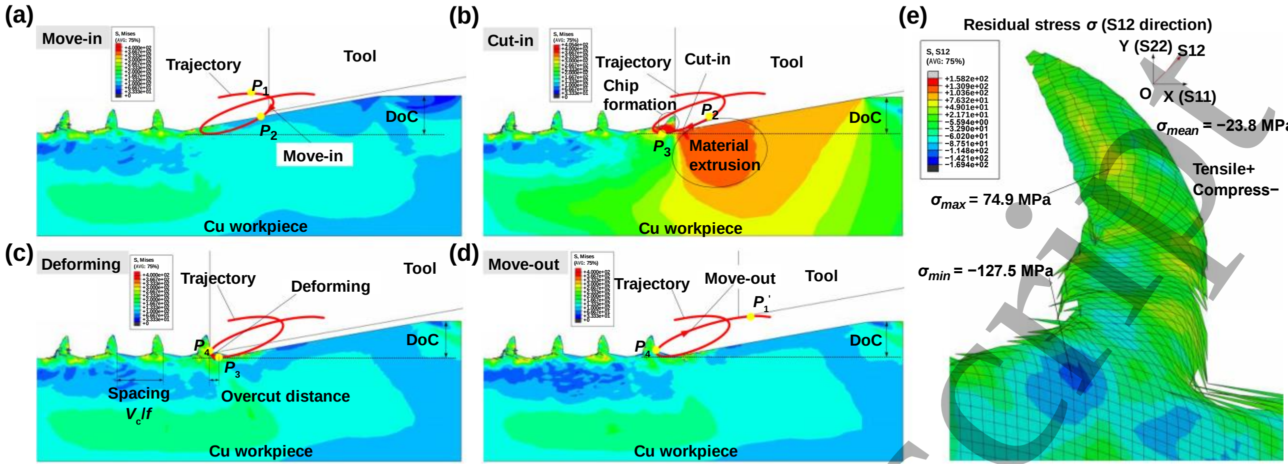

Figure 3. FEA of the microstructure's generation during EV-chiseling, including four steps. (a) Move-in step; (b) Cut-in step; (c) Deforming step; (d) Move-out step, and (e) residual stress of microstructure.

In addition to the tool vibration trajectory, the tool edge radius would have a great impact on the shear-dominated chip formation and the strength of the metallic structures. When the chip thickness is down to such a small scale, the scale effect could not be ignored[66], especially for the tool edge radius. During EV-chiseling, the tool edge radius can affect the chip formation in the Cut-in and Deforming steps. The smaller the tool edge radius is, the easier the chip separation; otherwise, the chip separation is more difficult. Also, from a molecular dynamics point of view[67], the smaller radius could reduce the force in the cutting process. Therefore, in the EV-chiseling process, the edge radius should be small enough.

2.3 Modeling the aspect ratio of textured microstructure

A mechanistic model is developed to establish the dependency of microstructures' shape on the process parameters, mainly based on the chip formation process in EV-chiseling. The general idea of model development is to differentiate the workpiece material into microelements, analyze the motion of each microelement of material, integrate them to derive the shape of the chip, and finally obtain the aspect ratio of the microstructures. As shown in **Figure 4**(a), C_{1i} denotes the positions of the i microelement of material before chiseling, while C_{2i} is its corresponding final position after chiseling. The critical modeling step is to determine the motion of each microelement of material from C_{1i} to C_{2i}.

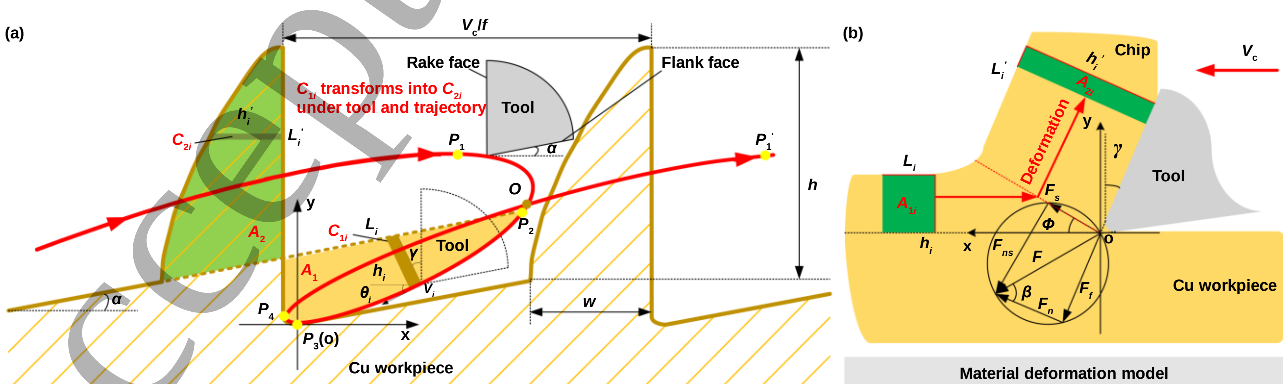

Figure 4. Model development. (a) A detailed generative model of microstructure for EV-chiseling. (b) Classic material deformation and flow model in chip formation.

The motion of the workpiece material stems from the material deformation and flow in EV-chiseling. Since EV-chiseling can be regarded as a particular cutting process with time-varying instantaneous DoC in each vibration cycle, the motion of the microelement of material in every moment complies with the classical cutting theory. **Figure 4**(b) shows a classic material deformation and flow model in cutting. The material deformation occurs in the shear zone ahead of the tool edge and flows along the tool rake face with a direction angle of γ+90°, and γ is the tool rake angle. The microelement of material with a cross-sectional area of A_{1i} is transformed into the microelement of the chip with a cross-sectional area of A_{2i}. Assuming material is not significantly compressed in the chip formation,

$$A_{1i} = A_{2i} \tag{6}$$

The relationship between the length L_i, L_i' and thickness h_i, h_i' of the microelement of material before and after deformation can be derived as,

$$\begin{cases} h_i' = \dfrac{h_i \cos(\Phi - \gamma)}{\sin \Phi} \\ L_i' = \dfrac{L_i \sin \Phi}{\cos(\Phi - \gamma)} \end{cases} \tag{7}$$

In **Eq. (7)**, Φ is the shear angle in cutting, which can be expressed as below according to Merchant's cutting theory[63, 68]:

$$\Phi = \frac{\pi}{4} - \frac{\beta}{2} + \frac{\gamma}{2} \tag{8}$$

where β is the friction angle on the tool rake face ($\beta = \tan^{-1} \mu$, μ is the friction coefficient between copper and diamond, $\mu = 0.2$ is used in this study). **Eq. (7-8)** indicates that the tool rake angle significantly affects the chip geometries after deformation in ordinary metal cutting.

However, the instantaneous tool rake angle changes with time in EV-chiseling due to elliptical tool vibration. To calculate the instantaneous tool rake angle, the tool motion in EV-chiseling is written as,

$$\begin{cases} x(t) = \sqrt{(a\cos\theta)^2 + (b\sin\theta)^2}\,\sin(2\pi ft) + V_c t \\ y(t) = \sqrt{(a\sin\theta)^2 + (b\cos\theta)^2}\,\sin(2\pi ft + \varphi) \end{cases} \tag{9}$$

where φ is the phase difference for two vibration directions.

Then, the instantaneous tool rake angle $\gamma(t)$ can be derived as,

$$\gamma(t) = \left|\theta(t)\right| = \left|\tan^{-1}\left(\frac{y'(t)}{x'(t)}\right)\right| \tag{10}$$

where $\theta(t)$ denotes the instantaneous cutting direction of the tool.

Next, the time-varying shear angle Φ can be obtained as,

$$\Phi(t)=\frac{\pi}{4}-\frac{1}{2}\beta+\frac{1}{2}\gamma(t) \tag{11}$$

Then, the height of chip h can be calculated by,

$$\begin{aligned} h&=\lim_{N\to\infty}\sum_{i=1}^{N}\frac{L_i'}{C_f}=\lim_{N\to\infty}\sum_{i=1}^{N}\frac{L_i}{C_f\cos\left(\Phi(t)-\gamma(t)\right)}\sin\Phi(t) \\ &=\int_{t_{P_2}}^{t_{P_4}}\frac{V\left(t\right)}{C_f\cos\left(\Phi(t)-\gamma(t)\right)}\sin\Phi(t)dt \end{aligned} \tag{12}$$

where t_{P2}, and t_{P4} are time when the tool reaches P_2, and P_4, which can be calculated easily by geometric method. C_f is the correction factor and $C_f = 2$. $V(t)$ is the instantaneous cutting velocity of the tool,

$$V\left(t\right)=\sqrt{\left(x'(t)\right)^2+\left(y'(t)\right)^2} \tag{13}$$

Then, the width of chip can be calculated by,

$$w=\max\left(C_f h_i'\right)=\max\left(\frac{C_f h_i\left(t\right)\cos\left(\Phi(t)-\gamma(t)\right)}{\sin\Phi(t)}\right) \tag{14}$$

where $h_i\left(t\right)$ is the thickness of material ahead of the tool on time t. α is the tool clearance angle and $\alpha = 10°$, the $h_i\left(t\right)$ can be derived by the simple geometric method as,

$$h_i\left(t\right)=\frac{\left|x(t)\tan\alpha-y(t)+V_c\tan\alpha/f\right|}{\sqrt{(1+\tan^2\alpha)}\cos(\left|\theta\left(t\right)\right|-\alpha)} \tag{15}$$

Finally, the aspect ratio of the microstructure can be obtained,

$$\text{Aspect ratio }=\frac{h}{w} \tag{16}$$

After finishing the above procedures, the shape and parameters of the microstructures could be derived for EV-chiseling. However, in EV-cutting, the mechanism of microstructure generation is not as complex as EV-chiseling. For comparison, the microstructure's geometries in EV-cutting are directly derived from the overlapping tool trajectories using classic models[36].

3. Experimental design

3.1 Experimental setup

Since the tool trajectory is critical for the efficacy of EV-chiseling, a 2D nonresonant vibration device is utilized to generate controllable elliptical vibration with large amplitude. As shown in **Figure 5**(a), two piezo stacks (PK4FQP1, Thorlabs) with a full stroke of 20 μm at 150 V are used to provide tool vibrations along two orthogonal directions. Two groups of spring hinges with proper wall thickness to satisfy the need for stiffness connect the piezo stack and end effector. The end effector is designed to be lightweight for a higher resonant frequency of the vibration device. Besides, the ball stud (RSU, VCN419-SS) and end cup (PKFCUP, Thorlabs) are used to properly mount the piezo stack (hemispherical head contacts hemispherical cup in the head and the tail direction) with excellent centrality. Finite element analysis (FEA) has been utilized in the design of the vibration device using ANSYS Workbench to determine its structural parameters. As a result, the first resonant mode frequency is 13 046 Hz and satisfies the process requirements. **Figure 5**(b) shows the static analysis results; the stiffness K of one handle is obtained as K is 12.7 $N\cdot\mu m^{-1}$, much smaller than the stiffness of the piezo stack, satisfying the requirement of piezo stack operation. A PC with LabVIEW generates the digital control signal of piezo stacks, which is transformed to the analog control signal by an NI DAQ board (NI PCIE 6361). With a shielded connecting box (NI BNC 2110) transferring, the control signals are amplified by two power amplifiers (PiezoDrive PX 200). The final input voltages and phases for the left and right piezo stack are denoted by U_L, U_R, Φ_L, and Φ_R. Two capacitive displacement sensors (MicroSense probe 5810, ADE 5514-LR-06) are used to measure the vibration amplitude as shown in **Figure 5**(c), and get the displacement and displacement phase as X, Y, φ_x, and φ_y for a fixed input frequency, respectively; the vibration amplitude in Y direction increases linearly with the input voltages, as shown in **Figure 5**(d). The vibration amplitude of different frequencies (100 ~ 6 000 Hz) of left and right handles along the handles' direction under the same voltage input shown in **Figure 5**(e), is highly stable: the amplitude fluctuation is less than 0.2 μm. Besides, the linear test has been done under different inputs voltage of 100 Hz and 1 000 Hz, with results showing that the two handles exhibit super-duper linearity, as shown in **Figure 5**(f). All the results demonstrate the actual superior performance of this device with large vibration amplitude under ultrafast vibration frequency (>1 kHz).

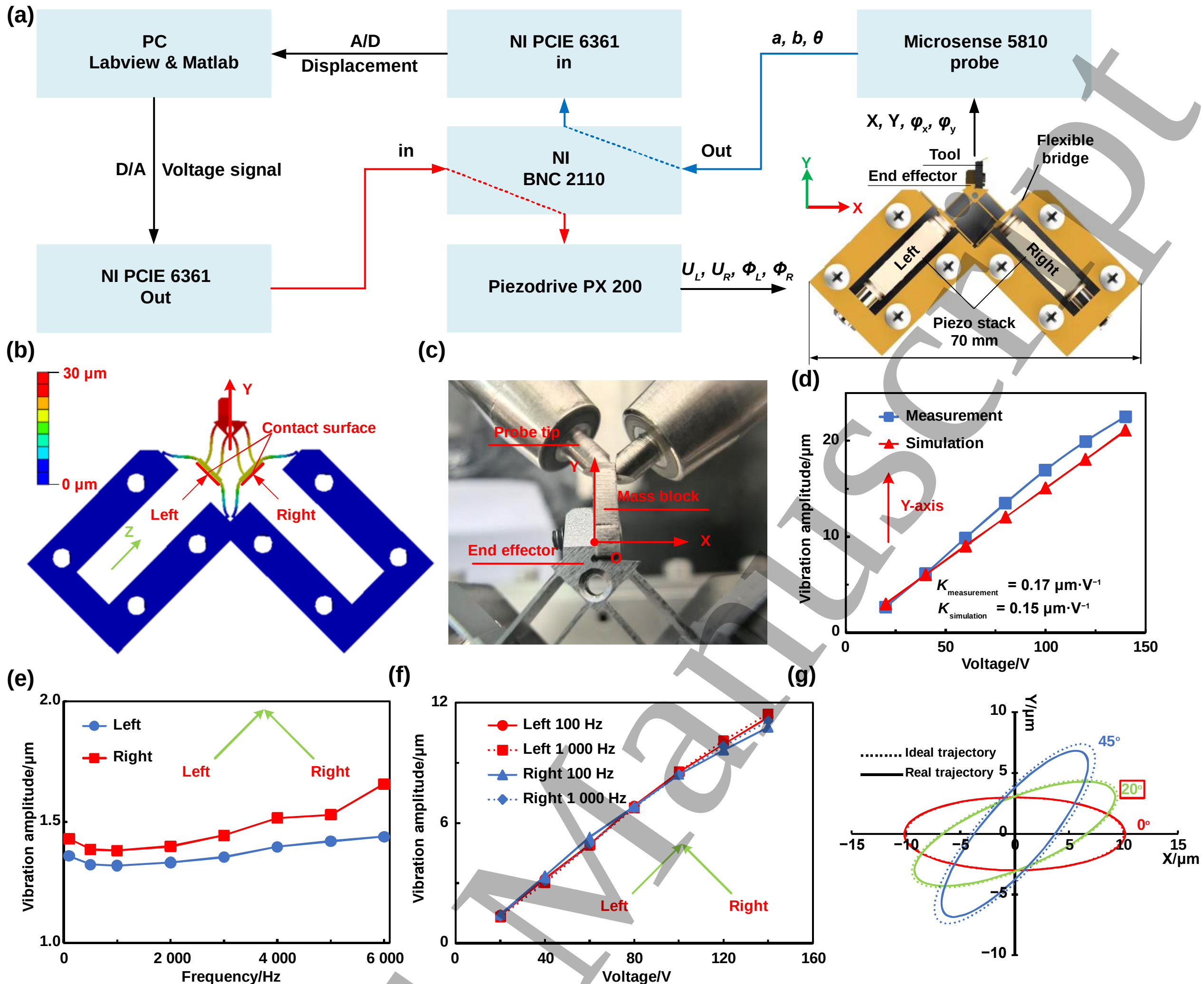

Figure 5. 2-D vibration device design and elliptical vibration trajectories control. (a) The schematic diagram for the working performance test platform; (b) statics analysis results; (c) measurement system of vibration amplitudes; (d) vibration amplitudes between measurement and simulation for different voltage input; (e)-(f): vibration amplitude test results for different frequency and voltage input; (g) elliptical vibration of ideal and real trajectories for different ellipses.

To accurately generate a controllable elliptical trajectory, the relationships among the control signal U_L, U_R, Φ_L, and Φ_R, and the axis's displacement X, Y, φ_x, and φ_y have been calibrated. The control signal and axis's displacement are assumed to have a linear relationship for nonresonant motion as follows:

$$\begin{bmatrix} Xe^{j\varphi_x} \\ Ye^{j\varphi_y} \end{bmatrix} = \begin{bmatrix} A_{xL}e^{j\delta_{xL}} & -A_{xR}e^{j\delta_{xR}} \\ A_{yL}e^{j\delta_{yL}} & A_{yR}e^{j\delta_{yR}} \end{bmatrix} \begin{bmatrix} U_L e^{j\phi_L} \\ U_R e^{j\phi_R} \end{bmatrix} \quad (17)$$

where A_{xL}, A_{xR}, and A_{yL}, A_{yR} are the related amplifying coefficients of the x and y axis, respectively, δ_{xL}, δ_{xR}, and δ_{yL}, δ_{yR} are the displacement offset phases of the x and y axis, respectively. The above parameters of the device are calibrated as shown in **Table 2**. The measured and designed typical ellipse ($a = 10$ μm, $b = 3$ μm, $\theta = 0°$, $20°$, and $45°$) are compared in **Figure 5**(g), and the deviation value is less than 0.5 μm. For smaller ellipses (a, $b < 5$ μm), the deviation value can be less than 0.1 μm, which satisfies the process requirement.

Table 2. Amplifying coefficients and displacement offset phases of the device (f = 1 000 Hz).

A_{xL}/μm.20V^{-1}	A_{yL}/μm.20 V^{-1}	A_{xR}/μm.20V^{-1}	A_{yR}/μm.20V^{-1}	δ_{xL}/rad	δ_{yL}/rad	δ_{xR}/rad	δ_{yR}/rad
1.26	0.92	1.28	0.88	2.997	3.002	3.002	3.004

A series of surface texturing tests were carried out using the self-developed 2D nonresonant vibration device on an ultraprecision platform to verify the efficacy of EV-chiseling, as shown in **Figure 6(**a) and (b). The ultraprecision platform (Aerotech, ANT 130+ACT 165) consists of a three-axis stage (X-, Y-, Z-axis) and a linear actuator (XX-axis). The self-developed 2D nonresonant vibration device is mounted on the linear actuator to provide the elliptical tool vibration. A single-point diamond tool is fixed on the end effector of the device. The detailed geometries of the diamond tool are shown in **Figure 6**(c)-(e)**.** The signal to actuate the vibration device is generated using LabVIEW, then transmitted to the power amplifier by the DAQ board. A copper workpiece is fixed on a two-axis inclination stage, which is used for level adjustment. The motion of the workpiece in the DoC and crossfeed direction is provided by the Y-axis and Z-axis stages, respectively, while the XX-axis actuator provides the nominal cutting motion of the tool. In addition, a digital camera (Leipan MS5, 100X) is used in situ to preset the tool's location and photograph the machining process.

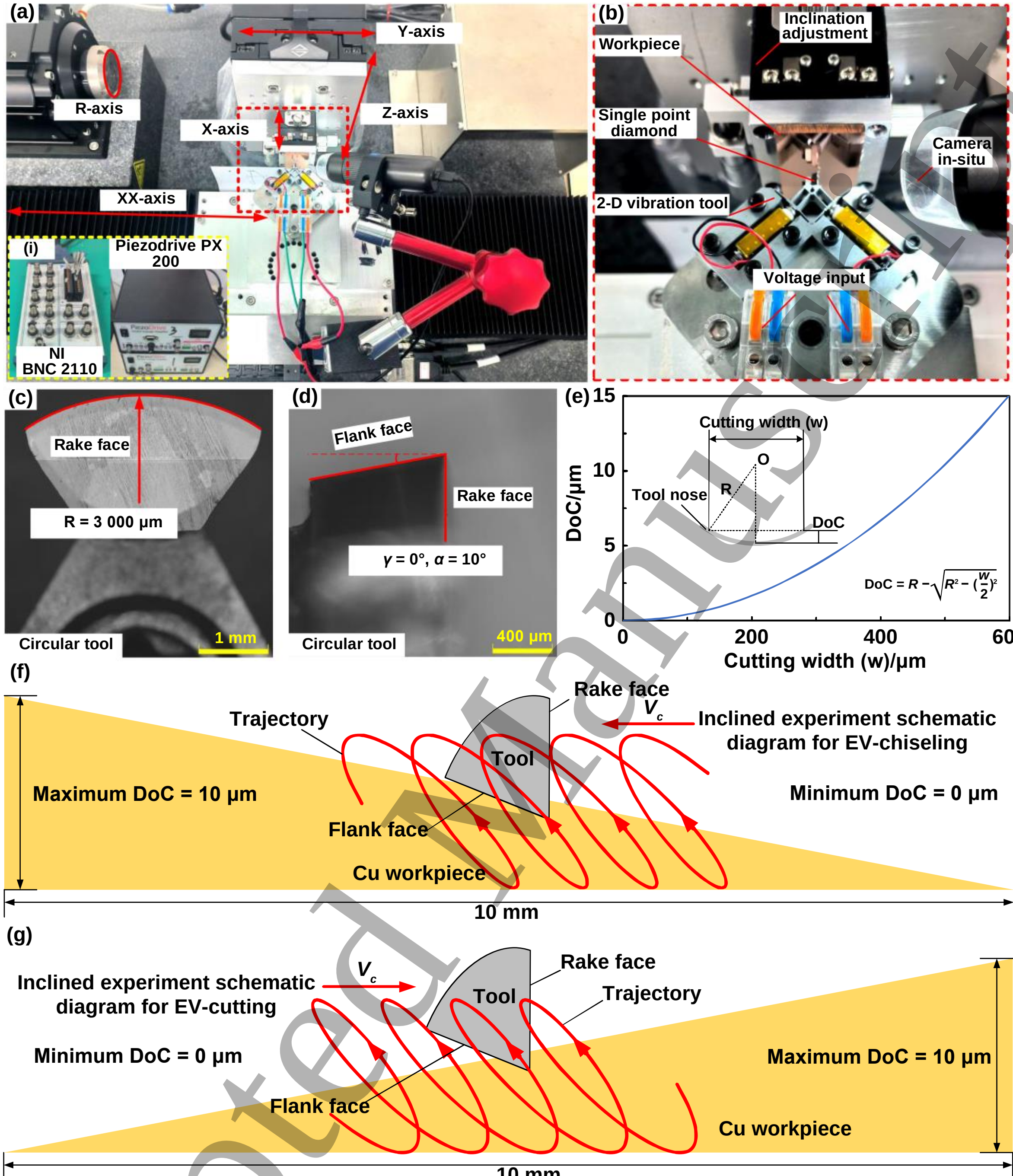

Figure 6. Experiment setup and diamond tool parameters. (a) The holistic perspective of the experiment; (b) detailed experiment setup; (c) front view of the circular diamond tool; (d) side view of the circular diamond tool; (e) the relationship between DoC and cutting width *w*; (f) the inclined experiment schematic diagram for EV-chiseling; (g) the inclined experiment schematic diagram for EV-cutting.

3.2 Process parameters and measurement methods

All the workpieces are flattened before the experiment. Both EV-chiseling and EV-cutting tests are conducted for comparison to demonstrate the capacity of EV-chiseling in the texturing of high-aspect-ratio microstructures. An inclined cutting method is used to explore the effects of DoC on the process performance for EV-chiseling and EV-cutting, as shown in **Figure 6**(f) and (g), respectively. During the texturing process, the DoC increases linearly from zero to 10 μm with a rate of 1 μm·mm^{-1}. The vibration ellipse is the same for all (a = 10, b = 3, θ = 20°), while the only difference is the cutting direction: the cutting direction for EV-chiseling is from left to right, but for EV-cutting is from right to left. The other process parameters are listed in **Table 3**. The other process parameters are listed in **Table 3**. Since V_c/f is equal to the spacing of microstructures, while f determines the generation rate of microstructures, V_c and f should be selected synergistically. The higher f is, the better to achieve high-efficiency; considering the bandwidth of the vibration device, f =1 000 Hz is used in this study. Hence, to texture microstructure with a spacing V_c/f ranging from 1 μm to 10 μm, the nominal cutting velocity V_c ranging from 1 to 10 mm·s^{-1} is used in the experiments. Parallelogram trajectory is also used in the experiment to explore the process potentials of vibration chiseling.

The tool geometries that affect the formed microstructures mainly include the clearance angle, edge radius, nose radius, rake angle, and edge inclination angle. The larger the tool clearance angle is, the better to reduce the interference tool trajectory with the unmachined surface. The tool edge radius determines the successful formation of microstructure through chiseling. A smaller edge radius is desirable to achieve smaller chip thickness. The tool nose radius, rake angle, and edge inclination angle are directly related to the geometries of the formed microstructures, enhancing the high flexibility of EV-chiseling process. Since this study focuses on the proposal and verification of the new process, the tool nose radius, rake angle, and edge inclination angle are not selected as the research variables. The circular diamond tool used in this study has a fixed nose radius of 3 mm, rake angle of 0°, clearance angle of 10°. Different cutting tools with different shapes and edge radius are used in the experiment. Single crystal diamond tools with circular, triangular, and rectangular shapes to illustrate the influence of tool shapes. A PCD (Polycrystalline diamond) tool in contrast with single diamond tools is used to show the effect of tool edge radius on the microstructure formation. An ultra-depth three-dimensional microscope (UDM, Hirox, HR-5000) is used to measure the tool edge radius. After the texturing tests, a laser scanning confocal microscope (LSCM, Olympus, LEXT OLS4100) and a scanning electron microscope (SEM, ZEISS, sigma 500) are used to measure the profile and morphology of the textured surface.

Table 3. Process parameters of EV-chiseling, EV-cutting, and parallelogram-shaped vibration-chiseling experiments.

No.	Process	Cutting velocity V_c /mm s^{-1}	Frequency f /Hz	Trajectory /μm	Cutting tool
1	EV-chiseling	5, 7	1 000	a = 10, b = 3, θ = 0 °	Circular tool
2	EV-chiseling	1, 2, 3, 4, 5, 6, 7, 8, 9, 10	1 000	a = 10, b = 3, θ = 20 °	Circular, Triangular, Rectangular, PCD tool
3	EV-chiseling	5, 7	1 000	a = 10, b = 3, θ = 45 °	Circular tool
4	EV-cutting	1, 2, 3, 4, 5, 6, 7, 8, 9, 10	1 000	a = 10, b = 3, θ = 20 °	Circular tool
5	Parallelogram-shaped vibration-chiseling	5, 7	100	Base = 13.7, height = 5, θ = 20 °	Circular tool

4. Results and discussion

4.1 Textured microstructure by EV-chiseling

The metallic microstructures with high aspect ratios have been successfully fabricated using EV-chiseling. **Figure 7** compares the surface morphologies of microstructures fabricated by EV-chiseling and EV-cutting. As shown in **Figure 7**(a), the EV-chiseling generates ribbed microstructures with good uniformity. The SEM figures clearly show the contrast between the microstructures' top (the light region) and bottom (the dark region). The top area is narrow, but the bottom is relatively wide. It is hard to observe the bottom of microstructures, especially for V_c is as tiny as 1 mm·s^{-1}. This is because the narrow-ribbed microstructures restrict light and electron access, which could find a broad application prospect in absorbing radiation, impurities, particles, cells, etc. The left and right surfaces of microstructure fabricated by EV-chiseling differ in smoothness. The left is vertical and smooth owing to its contact with the tool rake face, while the right is oblique and coarse with hierarchical structures caused by unconstrained material deformation. In contrast, as shown in **Figure 7**(b), the EV-cutting generates shallow grooves owing to tool vibration's reprojection effect. However, the uniformity of the textured structures by EV-chiseling is not as superior as EV-cutting. This is because chip deformation is more complicated than material removal in cutting. Some dynamic factors affect the chip deformation, such as the friction state between the chip and tool rake face. According to the general principle of metal cutting, the tool-chip friction significantly affects the shear angle in the first deformation zone, finally affecting the chip's length and thickness. A smaller friction coefficient should be beneficial to obtain microstructures with a higher aspect ratio. Hence, sufficient lubrication is essential for the EV-chiseling to create high-aspect-ratio microstructures with good uniformity.

The microstructures' surfaces are demonstrated in **Figure 8**(a) and (b), which quantitatively verify the efficacy of the proposed EV-chiseling in texturing high-aspect-ratio microstructures. For the same spacing of 6 μm, the height of chiseled microstructures is about 8 μm, about 16 times the height of the microstructure (0.5 μm) fabricated by EV-cutting. Moreover, the theoretical and measured results of the surface profiles are compared in **Figure 8**(c) and (d). Though deviations exist due to the elastic recovery of material[69], the theoretically predicted surface profiles agree well with the experimental results, verifying the developed model of microstructures' surface generation.

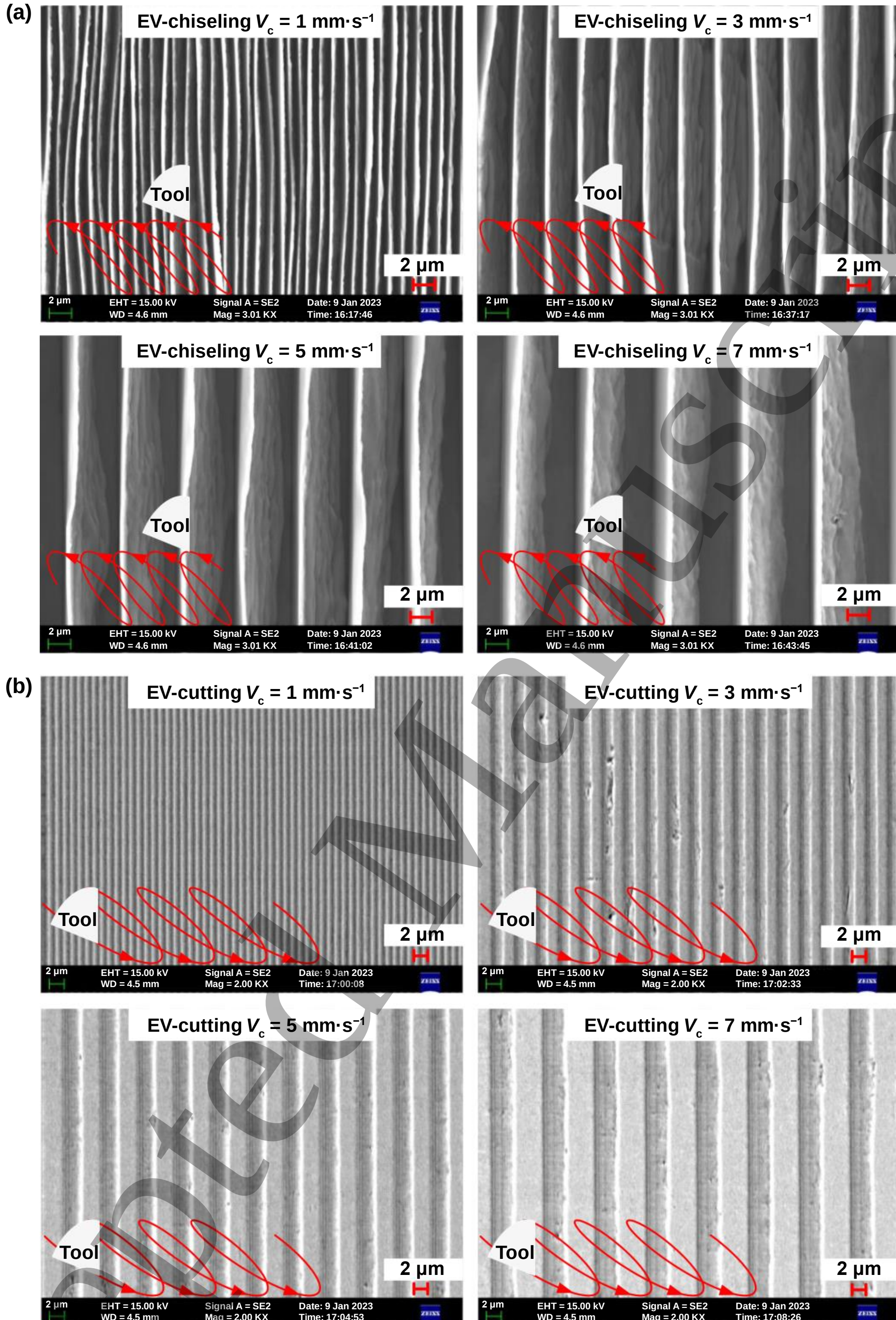

Figure 7. Typical machining SEM figures comparison between EV-chiseling and EV-cutting (DoC = 10 μm). (a) EV-chiseling results of different cutting velocity; (b) EV-cutting results of different cutting velocity. The oblique angle of the ellipse is 20°.

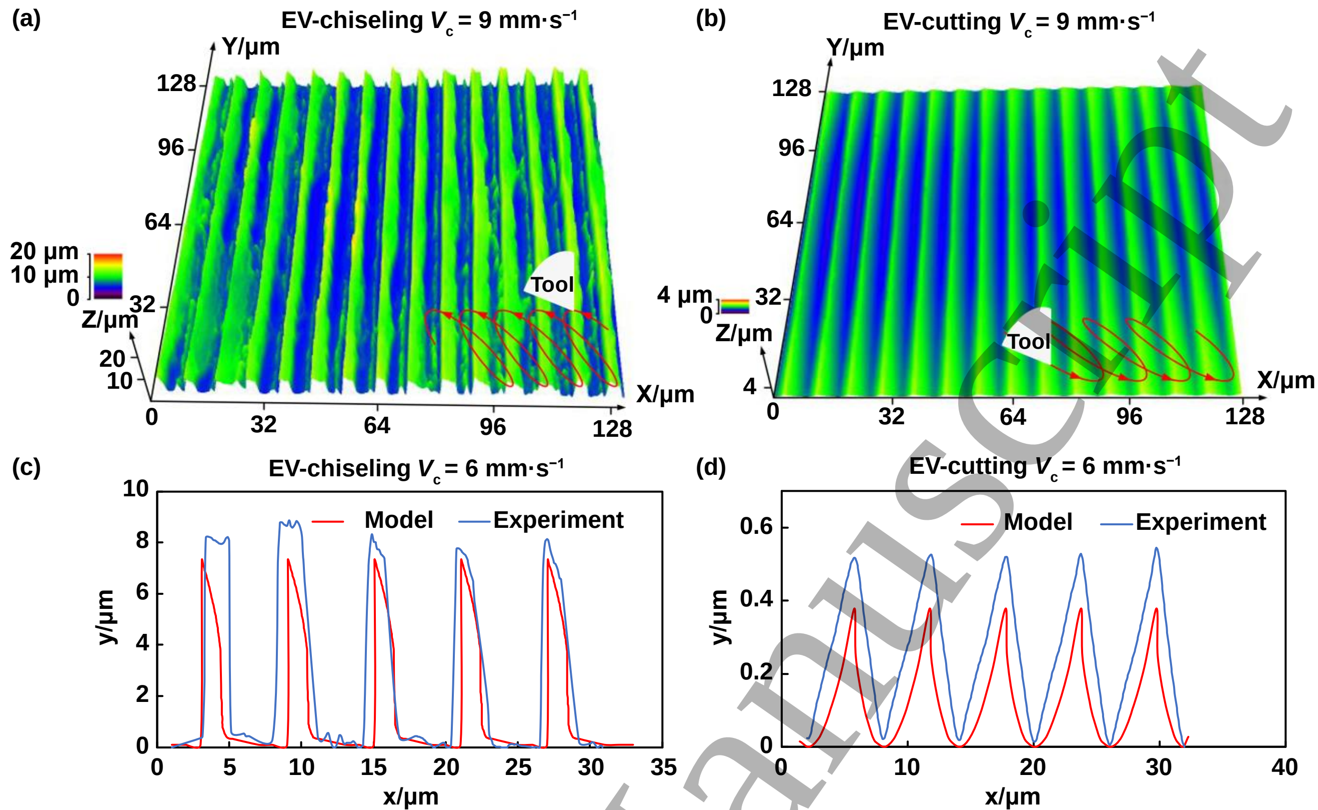

Figure 8. Typical machining surfaces (a) and (b) under V_c = 9 mm·s^{-1} and contrastive profiles (c) and (d) under V_c = 6 mm·s^{-1} between EV-chiseling and EV-cutting (DoC = 10 μm).

4.2 Comparison of aspect ratio among vibration texturing processes

The height, width, and aspect ratios of microstructures fabricated by EV-chiseling and EV-cutting under different microstructure spacing V_c/f are compared in **Figure 9**. EV-chiseling shows a much higher capacity to texture high-aspect-ratio microstructures than EV-cutting. Due to the limitation of the microscope, only the microstructure morphology with a relatively large spacing can be photographed clearly, taking V_c/f = 5 μm as the demarcation line. As shown in **Figure 9**(a) and (b)**,** the microstructure height by EV-chiseling is much larger than by EV-cutting, while the microstructure width by EV-chiseling is smaller than that by EV-cutting. As a result, the aspect ratio of microstructure by EV-chiseling is much larger than by EV-cutting, as shown in **Figure 9**(c). The maximum measured aspect ratio of microstructure by EV-chiseling is about 40 times that by EV-cutting.

In addition, the theoretically predicted height, width, and aspect ratios of microstructures by EV-chiseling agree well with the experimental results, further verifying the developed model of microstructures' surface generation. The microstructure height and width by both EV-chiseling and EV-cutting increase, if the microstructure spacing V_c/f increases. However, the aspect ratio of microstructure by EV-chiseling decreases with increasing V_c/f, which differs from EV-cutting. The derived aspect ratio of microstructure fabricated by EV-chiseling could be as high as 15 if V_c/f decreases to 1 μm, demonstrating that the proposed EV-chiseling can texture ultrahigh-aspect-ratio microstructures.

Moreover, the achieved aspect ratio by EV-chiseling and other cutting-based texturing methods including turning, milling, and fly cutting, in the literature is compared in **Figure 9(d)**. The more detailed data is listed in

Table 4. The maximum recorded aspect ratio of microstructures by other cutting-based texturing methods is 0.7[70]. In contrast, while maintaining high efficiency, the proposed EV-chiseling can texture microstructures with aspect ratios of >2, which can even be as high as 12, outperforming the existing cutting-based texturing methods.

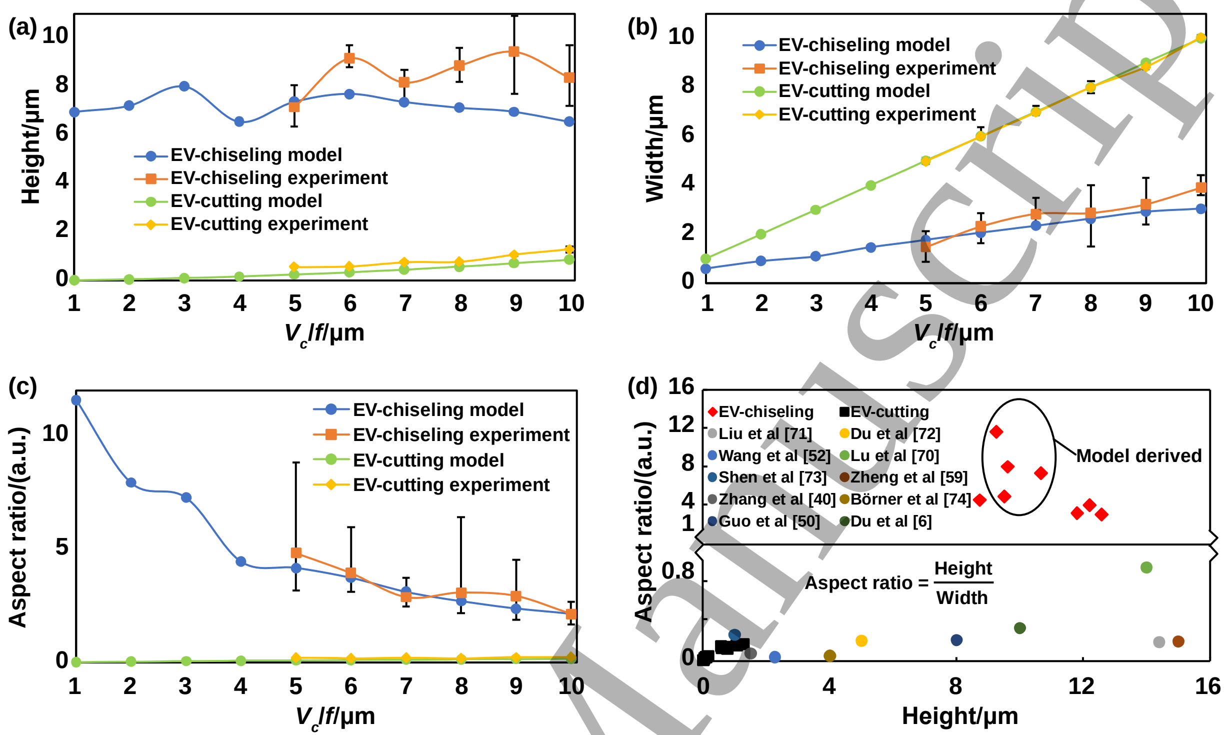

Figure 9. The comparison of the microstructure parameters for EV-chiseling and EV-cutting (DoC = 10 μm), the black short vertical line is the error bar of experimental results. (a) Height of the microstructures; (b) width of the microstructures; (c) aspect ratio of the microstructures, and each point is calculated by five microstructures; (d) distribution diagram of aspect ratio and height values from different literature; EV-chiseling shows the highest aspect ratio (upper region).

Table 4. Contrast height, width, and aspect ratio from different representative literature.

Original literature	Process	Height/μm	Width/μm	Aspect ratio/ (a.u.)
Liu *et al.*[71]	Turning	14.40	98.90	0.15
Du *et al.*[72]	Planning	5.00	32.30	0.15
Wang *et al.*[52]	Turning	2.27	69.10	0.03
Lu *et al.*[70]	Milling	14.00	20.00	0.70
Shen *et al.*[73]	Milling	1.00	5.00	0.20
Zheng *et al.*[59]	Milling	15.00	100.00	0.15
Zhang *et al.*[40]	Fly cutting	1.50	25.00	0.06
Börner *et al.*[74]	Milling	4.00	95.00	0.04
Guo *et al.*[50]	Planning	8.00	50.00	0.16
Du *et al.*[6]	Planning	10.00	40.00	0.25

4.3 Effects of elliptical and parallelogram trajectories

The tool vibration trajectory plays a critical role in ensuring the efficacy of EV-chiseling. **Figure 10** compares the morphology of textured surfaces by vibration chiseling using standard, inclined elliptical and parallelogram trajectories. As shown in **Figure 10**(a) and (b), shallow microstructures are created on the surface if a standard elliptical trajectory is used, which is explained in **Figure 10**(c). In this case, **Eq. 5** that guarantees the transformation of the chip to the surface microstructure is not satisfied. In each vibration cycle, the tool overcut distance is larger than the microstructure spacing, leading to the breakage, and falling from the chip rather than transforming to the microstructures. In contrast, if an inclined elliptical trajectory ($\theta = 45°$) is used to satisfy **Eq. 5**, high-aspect-ratio microstructures are successfully fabricated, as shown in **Figure 10**(d)-(f).

Moreover, vibration chiseling shows high process flexibility by modifying the tool trajectories. The applicable tool trajectory for vibration chiseling is not limited to elliptical. Parallelograms[75], triangles, or other nonharmonic trajectories that satisfy the microstructure generation condition can also be adopted in vibration chiseling. **Figure 10**(g)-(i) demonstrate the textured surface using a parallelogram trajectory, which shows that high-aspect-ratio microstructures are fabricated by transforming the chip into microstructures. It is worth noting that the textured microstructures show a cured shape when the microstructure spacing V_c/f is 5 μm, which could find an array of breakthrough applications like directional droplet transport due to its unique characteristics. These curved microstructures are challenging to fabricate by other methods, demonstrating the unique process capacity of vibration chiseling.

In addition, the vibration amplitudes of elliptical trajectory critically affect the achievable maximum aspect ratio of the microstructures. A larger vibration amplitude in both the vertical and horizontal directions is beneficial to create high structures. However, due to the structure is generated through the material deformation, metallographical evolution may occur in both microstructures and the Cu workpiece. Though the metallographical evolution of Cu workpiece is inevitable, reducing the tool clearance angle can mitigate the surface alterations. These evolutions on the textured microstructures could have either detrimental or beneficial effects. On the one hand, residual stress might diminish the strength of structure. On the other hand, the potential grain refinement may enhance corrosion resistance.

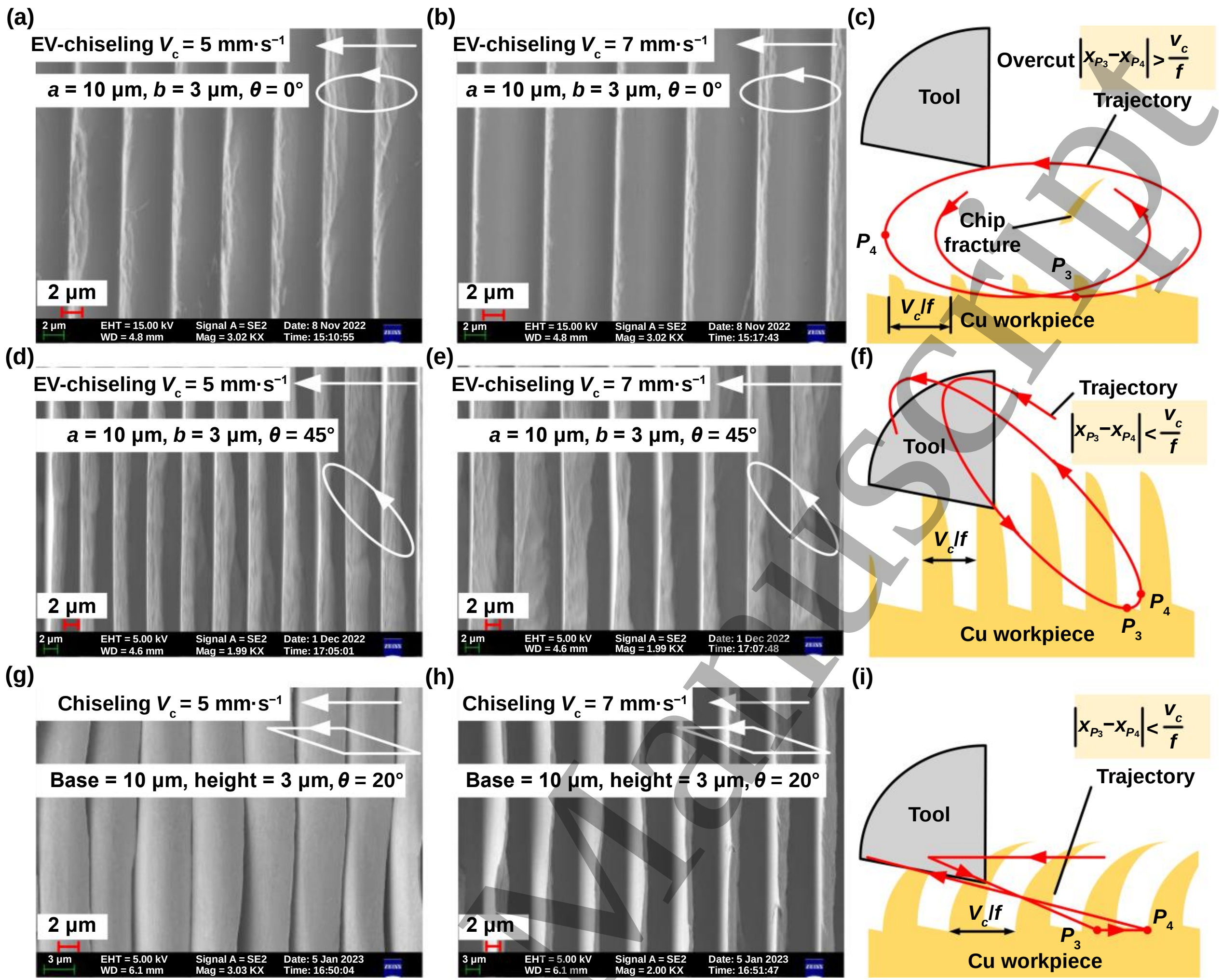

Figure 10. The typical machining SEM figures and diagram comparison between different loci for vibration chiseling (DoC = 10 μm). (a)-(c): 0° standard ellipse; (d)-(f): 45° oblique ellipse; (g)-(i): parallelogram. The cutting direction is from right to left, the scale bar is 2 μm for all sub-figures.

4.4 Effects of different DoC

The DoC also significantly affects the surface generation of microstructure in EV-chiseling. **Figure 11** shows the results of grooving experiments using a circular tool. The nominal cutting velocity is 8 mm·s^{-1}, and the cutting direction is from right to left. The actual DoC at a selected position is calculated by the measured structure length *w* using **Figure 6**(e). According to **Eq. 18**, due to the interaction between the tool clearance face and workpiece, there should exist a critical DoC, below which the height of the textured microstructure increases with the increasing DoC. If the DoC is larger than the critical value, the shape of the microstructure tends to be unchanged. The experimental results support the above analysis. The calculated critical DoC is 1.6 μm. Therefore, uniform ribbed microstructures with similar shape are fabricated when DoC = 4.1, 7.3, and 9.2 μm.

$$\mathrm{DoC} \geq \left| y_O - y_{P_3} \right| \tag{18}$$

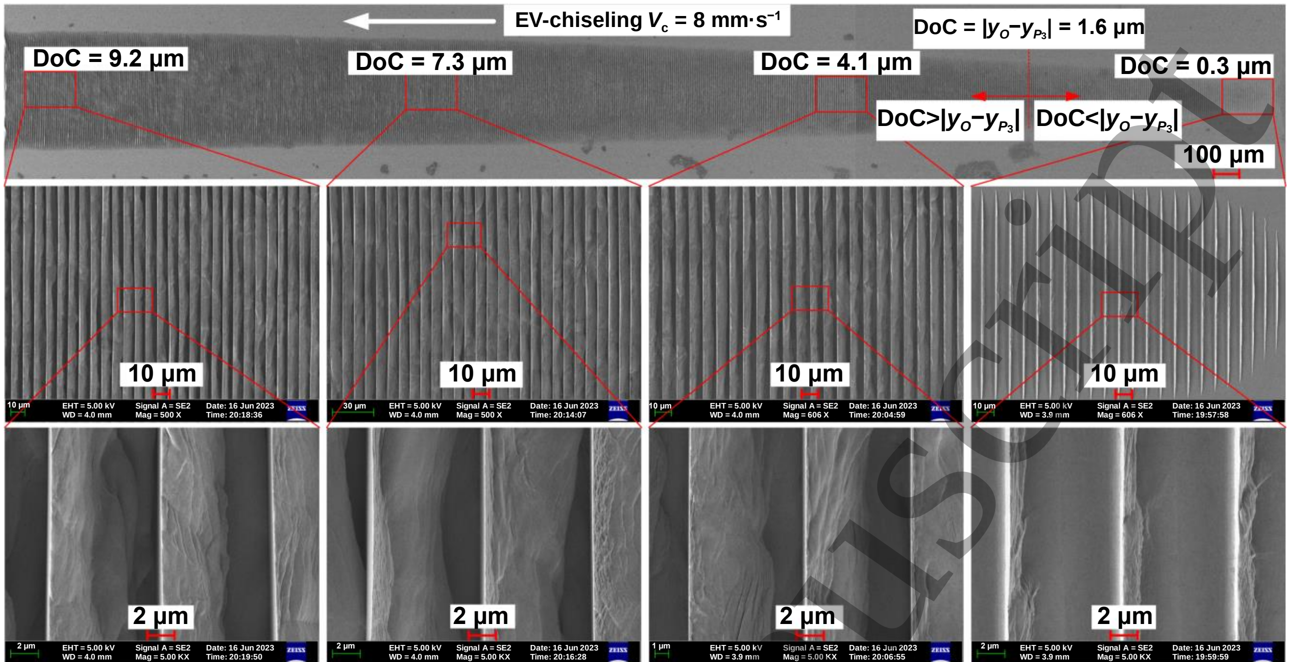

Figure 11. The typical machining SEM figures of microstructures under different DoC for EV-chiseling. The cutting direction is from right to left.

4.5 Textured surface using different cutting tools

The tool nose's shape is another important factor determining the microstructures' geometries textured by EV-chiseling. **Figure 12** shows the fabricated microstructures by EV-chiseling using a triangular and rectangular tool, respectively. The tool nose's shape mainly determines the cross-sectional profile of the textured groove. As shown in **Figure 12**, triangle-shaped and rectangle-shaped grooves with uniform ribbed microstructures are created on the workpiece surface. The aspect ratio of ribbed microstructure can be as high as 7. The ribbed microstructure's length is usually coupled with the DOC using a triangular or circular tool. However, if using a rectangular tool, the ribbed microstructure's length is a constant that is the same as the tool's width. This decoupling of the microstructure's length to the height can enable the more flexible control of the geometries and distribution of the microstructures by EV-chiseling.

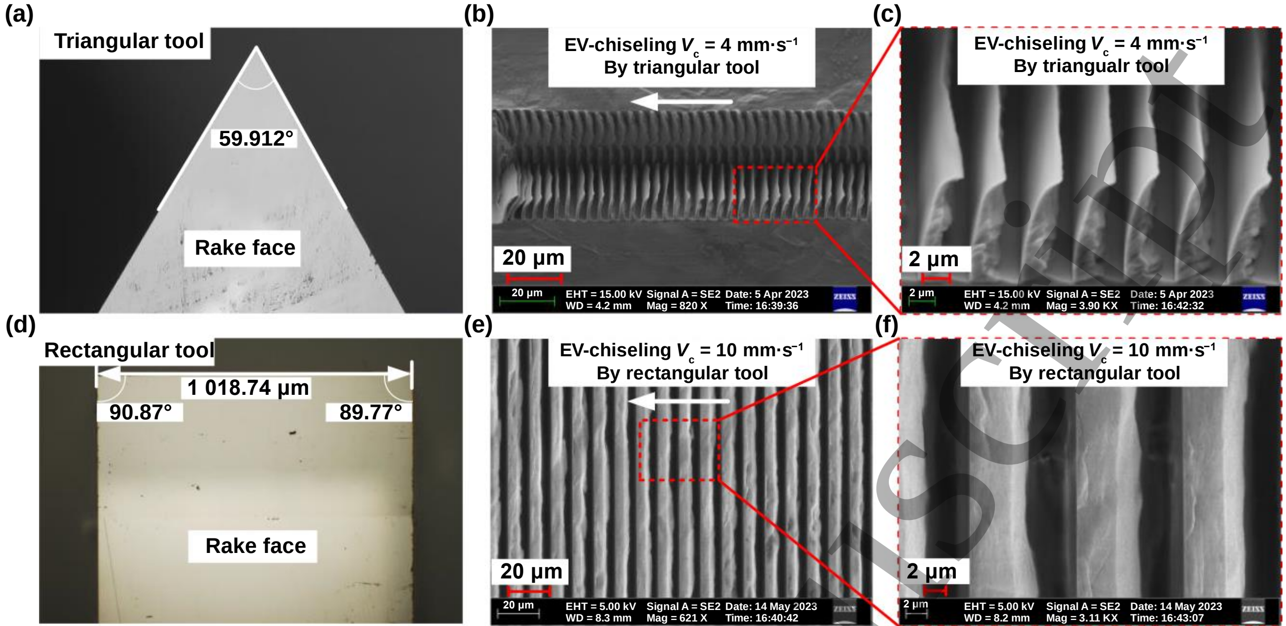

Figure 12. Typical machining SEM figures between different diamond tools for EV-chiseling (DoC = 10 μm). (a)-(c): triangular tool; (d)-(f): rectangular tool. The cutting direction is from right to left.

4.6 Effects of tool edge radius

The tool edge radius plays a critical role in determining the successful execution of EV-chiseling. To demonstrate the critical effects of tool edge radius, a PCD tool with an edge radius of 8 μm (as shown in **Figure 13**, much larger than the diamond tool's edge radius of 100 nm) has been used to conduct the EV-chiseling process. The surface morphologies of the textured microstructures using the PCD tool are listed in **Figure 14.** As shown in **Figure 14**, though periodic microstructures can also be produced on the surface, they are very shallow. Ribbed microstructures are not successfully generated, indicating the failure of the process principle in EV-chiseling. This is because the edge radius is closely related to the minimum chip thickness in metal cutting. According to Guo *et al*.[76], the undeformed chip thickness should be larger than 0.16 times the tool edge radius to enable a successful chip formation from the surface. When the tool edge radius is 8 μm, the minimum chip thickness is about 1.3 μm, which is too close to the microstructure spacing to generate a chip ahead of the tool rake face. Moreover, with the increase of tool edge radius, the cutting force is assumed to increase significantly, which might destroy and remove the chip from the surface. However, a small tool edge radius might violate the tool's life due to inevitable tool wear. Hence, if considering the tool life, there exists a maximum acceptable tool edge radius to guarantee the efficacy of EV-chiseling, which depends on the workpiece material, tool vibration trajectory, and other processing parameters. If neglecting the tool wear, the sharper tool edge is, the better to increase the efficacy of EV-chiseling.

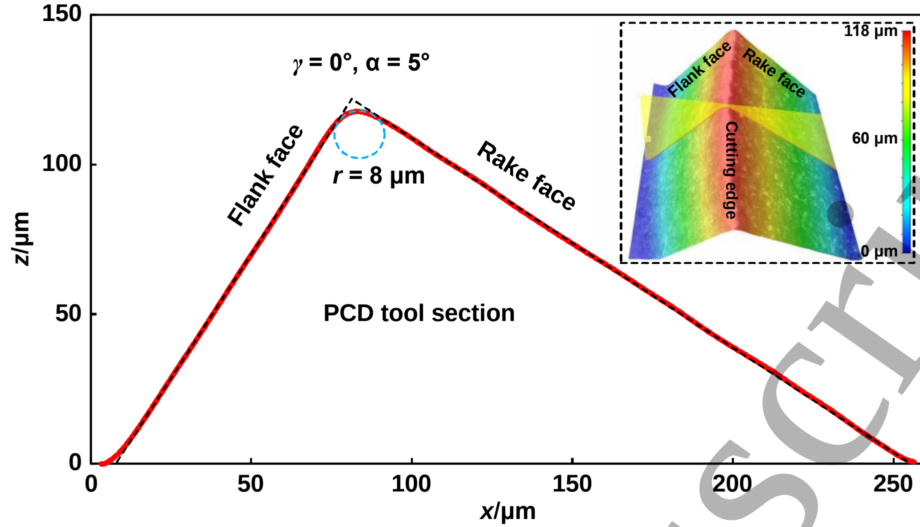

Figure 13. The section and morphology of PCD tool.

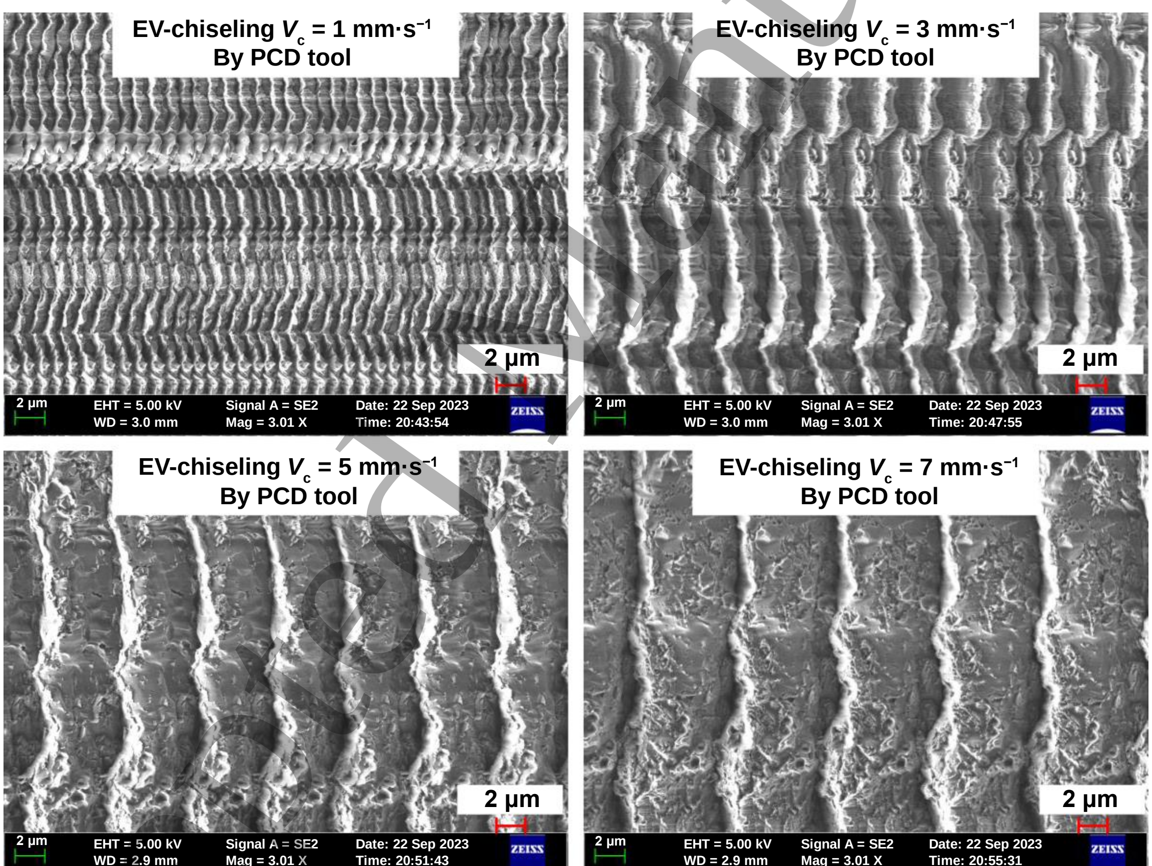

Figure 14. Typical SEM figures of microstructures textured by EV-chiseling using PCD tool (DoC = 10 μm, the oblique angle of the ellipse is 20°).

It is worth noting that the determination of process parameters is ultimately based on the application performance of textured microstructures. The optimum geometries of textured structure in EV-chiseling vary with the different applications, such as heat transfer enhancement, antibiosis, and grating-coupled surface plasmon. Though we have already explored the relationship between the process parameters and structure geometries, establishing the complete links between the process parameters, structure geometries/properties and application performance are essential for further study.

5. Conclusions

This study invents an EV-chiseling process to enable the fast and cost-effective fabrication of ultra-high-aspect-ratio microstructures on metallic surfaces. FEA is performed to explore the process mechanics in EV-chiseling. A process model is established to describe the relationship between the microstructures' geometries and the process inputs. Surface texturing tests are conducted using a self-developed vibration device to verify EV-chiseling's efficacy and developed process model. The specific conclusions are as follows:

(1) The key principle of EV-chiseling relies on the elliptical tool vibration and the backward tool moving direction. The tool chisels into the material in each vibration cycle to generate an upright chip through material deformation. The chip is left on the material surface rather than falling off to form a ribbed microstructure with a high aspect ratio.

(2) Uniformed microstructures with an aspect ratio of 2 ~ 12 in the spacing scale of 1 ~ 10 μm have been successfully fabricated using EV-chiseling. Compared to EV-cutting with a forward-moving tool, the aspect ratio of microstructures increases by 40 times. EV-chiseling outperforms the existing cutting-based texturing methods in the literature.

(3) The developed process model of EV-chiseling has been verified by the measured results of the microstructures' geometric parameters, including the height, width, and aspect ratio. Both the model-predicted and experimental results demonstrate that the microstructure's height and width increase, while the aspect ratio of the microstructure decreases with increasing microstructures' spacing under the same DoC.

(4) The tool vibration trajectory plays a critical role in ensuring the efficacy of EV-chiseling. Compared to the inclined elliptical trajectory, the standard elliptical trajectory is unsuitable for EV-chiseling. Besides, the applicable tool trajectory for the general vibration chiseling is not limited to elliptical. Arbitrary nonharmonic trajectories like parallelogram that satisfy the microstructure generation condition can be adopted to enable the high process flexibility of vibration chiseling.

(5) The DoC, tool nose's shape, and tool edge radius also affect the surface generation of microstructure in EV-chiseling. There should exist a critical DoC, above which the microstructure height tends to be unchanged due to the interaction between the tool clearance face and the workpiece. The tool nose's shape mainly determines the cross-sectional profile of the textured groove. If using a rectangular tool, the ribbed microstructure's length is decoupled with the DoC, bringing a more flexible control of the geometries of the microstructures by EV-chiseling. The tool cutting edge radius should be as small as possible to fabricate high aspect ratio microstructures.

Acknowledgments

The authors gratefully acknowledge the financial support for this research provided by the National Natural Science Foundation of China (Grant No. 52105458); Beijing Natural Science Foundation (Grant No. 3222009);

Huaneng Group Science and Technology Research Project (No: HNKJ22-H105); China Postdoctoral Science Foundation (Grant No: 2022M711807).

References

[1] Xuan Z Y, Li J Y, Liu Q Q, Yi F, Wang S W and Lu W. 2021. Artificial structural colors and applications. *Innovation* **2**, 100081.

[2] Mori S and Utaka Y. 2017. Critical heat flux enhancement by surface modification in a saturated pool boiling: a review. *Int. J. Heat Mass Transfer* **108**, 2534-2557.

[3] Higgins S G, Becce M, Belessiotis-Richards A, Seong H, Sero J E and Stevens M M. 2020. High-aspect-ratio nanostructured surfaces as biological metamaterials. *Adv. Mater.* **32**, 1903862.

[4] Wang W, He Y Y, Zhao J, Mao J Y, Hu Y T and Luo J B. 2020. Optimization of groove texture profile to improve hydrodynamic lubrication performance: theory and experiments. *Friction* **8**, 83-94.

[5] Gimeno S, Mescheder H, Quintana I, Gasión A, Arias-Egido E, Carbonell A, Mallo C, Miguel I, Paredes J and Zalakain I. 2023. Effect of different laser texturing patterns on rolling contact surface and its tribological & fatigue life behavior on 100Cr6 bearing steel. *Wear* **522**, 204717.

[6] Du H H, Zhu Z W, Wang Z K and To S. 2023. Fabrication of high-aspect-ratio and hierarchical micro/nanostructure arrays by a novel piezoelectrically actuated cutting system. *Mater. Des.* **226**, 111660.

[7] Long J Y, Liu Z Y, Lin H P, Li Y, Cao Z, Zhang Z C and Xie X Z. 2022. Pool boiling heat transfer and bubble dynamics over V-shaped microchannels and micropyramids: does high aspect ratio always benefit boiling?. *Appl. Therm. Eng.* **201**, 117796.

[8] He Y, Yan Y D, Geng Y Q and Brousseau E. 2018. Fabrication of periodic nanostructures using dynamic plowing lithography with the tip of an atomic force microscope. *Appl. Surf. Sci.* **427**, 1076-1083.

[9] Anscombe N. 2010. Direct laser writing. *Nat. Photonics* **4**, 22-23.

[10] Feinaeugle M, Pohl R, Bor T, Vaneker T and Römer G W. 2018. Printing of complex free-standing microstructures via laser-induced forward transfer (LIFT) of pure metal thin films. *Addit. Manuf.* **24**, 391-399.

[11] Tong H, Li Y, Wang Y and Yu D W. 2008. Servo scanning 3D micro-EDM based on macro/micro-dual-feed spindle. *Int. J. Mach. Tools Manuf.* **48**, 858-869.

[12] Wu B Q, Kumar A and Pamarthy S. 2010. High aspect ratio silicon etch: a review. *J. Appl. Phys.* **108**, 051101.

[13] Chang B D, Leussink P, Jensen F, Hübner J and Jansen H. 2018. DREM: infinite etch selectivity and optimized scallop size distribution with conventional photoresists in an adapted multiplexed Bosch DRIE process. *Microelectron. Eng.* **191**, 77-83.

[14] Palneedi H *et al.* 2018. Laser irradiation of metal oxide films and nanostructures: applications and advances. *Adv. Mater.* **30**, 1705148.

[15] Zhang D S, Liu R J and Li Z G. 2022. Irregular LIPSS produced on metals by single linearly polarized femtosecond laser. *Int. J. Extrem. Manuf.* **4**, 015102.

[16] Zhu Q C, Fan P X, Li N, Carlson T, Cui B, Silvain J F, Hudgins J L and Lu Y F. 2021. Femtosecond-laser sharp shaping of millimeter-scale geometries with vertical sidewalls. *Int. J. Extrem. Manuf.* **3**, 045001.

[17] Buividas R, Rekštytė S M, Malinauskas M and Juodkazis S. 2013. Nano-groove and 3D fabrication by controlled avalanche using femtosecond laser pulses. *Opt. Mater. Express* **3**, 1674-1686.

[18] Bonse J, Höhm S, Kirner S V, Rosenfeld A and Krüger J. 2017. Laser-induced periodic surface structures—A scientific evergreen. *IEEE J. Sel. Top. Quantum Electron.* **23**, 9000615.

[19] Gu D D, Shi X Y, Poprawe R, Bourell D L, Setchi R and Zhu J H. 2021. Material-structure-performance integrated laser-metal additive manufacturing. *Science* **372**, eabg1487.

[20] Bellotti M, De Eguilior Caballero J R, Qian J and Reynaerts D. 2021. Effects of partial tool engagement in micro-EDM milling and adaptive tool wear compensation strategy for efficient milling of inclined surfaces. *J. Mater. Process. Technol.* **288**, 116852.

[21] Li L G, Wang P T, Shao Q and Huang X Q. 2020. Metallic nanostructures with low dimensionality for electrochemical water splitting. *Chem. Soc. Rev.* **49**, 3072-3106.

[22] Zhang Q, Li P S, Zhou D J, Chang Z, Kuang Y and Sun X M. 2017. Superaerophobic ultrathin Ni–Mo alloy nanosheet array from in situ topotactic reduction for hydrogen evolution reaction. *Small* **13**, 1701648.

[23] Kuang Y, Feng G, Li P S, Bi Y M, Li Y P and Sun X M. 2016. Single-crystalline ultrathin nickel nanosheets array from in situ topotactic reduction for active and stable electrocatalysis. *Angew. Chem. Int. Ed.* **55**, 693-697.

[24] Zhu D and Zeng Y B. 2008. Micro electroforming of high-aspect-ratio metallic microstructures by using a movable mask. *CIRP Ann.* **57**, 227-230.

[25] Zhou B, Su B, Li M and Meng J H. 2020. Microelectroforming of freestanding metallic microcomponents using silver-coated poly(dimethylsiloxane) molds. *J. Micromech. Microeng.* **30**, 045013.

[26] Li M, Liu J, Zhang X P, Tian Y Q and Jiang K. 2018. Fabrication of graphene/nickel composite microcomponents using electroforming. *Int. J. Adv. Manuf. Technol.* **96**, 3191-3196.

[27] Liu J, Hassanin H, Ni Z Y, Yang Y, Yang G and Jiang K. 2017. Production of high-precision micro metallic components by electroforming process. *Mater. Manuf. Process.* **32**, 1325-1330.

[28] Kuang P, Park J M, Leung W, Kim T G, Ho K M and Constant K. 2010. High aspect ratio nanoscale metallic structures as transparent electrodes. *In Proc. SPIE 7756, Active Photonic Materials III*. 77560M. (SPIE, San Diego, CA, USA).

[29] Kang M G, Kim M S, Kim J and Guo L J. 2008. Organic solar cells using nanoimprinted transparent metal electrodes. *Adv. Mater.* **20**, 4408-4413.

[30] Kang M G and Guo L J. 2007. Nanoimprinted semitransparent metal electrodes and their application in organic light-emitting diodes. *Adv. Mater.* **19**, 1391-1396.

[31] Li H C, Tang H, Li J D and Chen X. 2021. Design, fabrication, and testing of a 3-DOF piezo fast tool servo for microstructure machining. *Precis. Eng.* **72**, 756-768.

[32] Zhou T F, Zhou J, Wang T X, Gao L H, Ruan B S, Yu Q, Zhao W X and Wang X B. 2022. Fabrication of high aspect-ratio aspheric microlens array based on local spiral diamond milling. *J. Manuf. Process.* **83**, 547-554.

[33] Jiang M N *et al*. 2022. Inhibiting the Leidenfrost effect above 1,000 °C for sustained thermal cooling. *Nature* **601**, 568-572.

[34] Zhou J, Zhou T F, Wang T X, Ruan B S, Zhao W X and Wang X B. 2023. Study on the tool setting for microlens array machining via swing cutting. *J. Manuf. Process.* **85**, 636-644.

[35] Miao Q, Ding W F, Xu J H, Cao L J, Wang H C, Yin Z, Dai C W and Kuang W J. 2021. Creep feed grinding induced gradient microstructures in the superficial layer of turbine blade root of single crystal nickel-based superalloy. *Int. J. Extrem. Manuf.* **3**, 045102.

[36] Shamoto E and Moriwaki T. 1994. Study on elliptical vibration cutting. *CIRP Ann.* **43**, 35-38.

[37] Kong L B and Cheung C F. 2012. Modeling and characterization of surface generation in fast tool servo machining of microlens arrays. *Comput*. *Ind*. *Eng*. **63**, 957-970.

[38] Pratap T and Patra K. 2018. Fabrication of micro-textured surfaces using ball-end micromilling for wettability enhancement of Ti-6Al-4V. *J*. *Mater*. *Process*. *Technol*. **262**, 168-181.

[39] de Oliveira D, Gomes M C, de Oliveira G V, dos Santos A G and da Silva M B. 2021. Experimental and computational contribution to chip geometry evaluation when micromilling Inconel 718. *Wear* **476**, 203658.

[40] Zhang G Q, Ma S, Wang J P, Jiang J K, Luo T and Wang H T. 2022. Offset-tool-servo diamond end flycutting multi-layer hierarchical microstructures. *Int*. *J*. *Mech*. *Sci*. **233**, 107645.

[41] Huang Y, Huang J C, Xiao G J, Lin O C, Liu S, Liu Z Y and Wu C J. 2023. Morphology and wettability analysis of square micropillar structure prepared by laser-belt machining on Inconel 718 alloy surface. *Int*. *J*. *Adv*. *Manuf*. *Technol*. **127**, 3919-3933.

[42] Yang Z C, Zhu L D, Zhang G X, Ni C B and Lin B. 2020. Review of ultrasonic vibration-assisted machining in advanced materials. *Int*. *J*. *Mach*. *Tools Manuf*. **156**, 103594.

[43] Zhang J G, Cui T, Ge C, Sui Y and Yang H J. 2016. Review of micro/nano machining by utilizing elliptical vibration cutting. *Int*. *J*. *Mach*. *Tools Manuf*. **106**, 109-126.

[44] Yang J C, Feng P F, Zhang J F, Yang H L and Wang J J. 2023. On the oxidation resistance of sinusoidal microstructure fabricated by elliptical vibration cutting. *Surf*. *Coat*. *Technol*. **459**, 129370.

[45] Wang J J, Du H H, Gao S M, Yang Y, Zhu Z W and Guo P. 2019. An ultrafast 2-D non-resonant cutting tool for texturing micro-structured surfaces. *J*. *Manuf*. *Process*. **48**, 86-97.

[46] Zhang H W, Feng P F, Feng F, Zhang J F, Wang C J and Wang J J. 2023. Structural coloration with two-dimensional nanostructures fabricated by elliptical vibration nanoindentation. *Precis*. *Eng*. **82**, 219-232.

[47] Chen K Y, Si C and Guo P. 2017. Design of a high bandwidth nonresonant tertiary motion generator for elliptical vibration texturing. *J*. *Micro Nano-Manuf*. **5**, 011008.

[48] Guo P and Ehmann K F. 2013. Development of a tertiary motion generator for elliptical vibration texturing. *Precis*. *Eng*. **37**, 364-371.

[49] Kurniawan R, Kiswanto G and Ko T J. 2016. Micro-dimple pattern process and orthogonal cutting force analysis of elliptical vibration texturing. *Int*. *J*. *Mach*. *Tools Manuf*. **106**, 127-140.

[50] Guo P and Ehmann K F. 2013. An analysis of the surface generation mechanics of the elliptical vibration texturing process. *Int*. *J*. *Mach*. *Tools Manuf*. **64**, 85-95.

[51] Chen Z M, Feng P F, Zhang J F, Feng F, Zhang H W, Yu J H and Wang J J. 2023. Shaped vibration cutting: a novel fabrication method for mid-infrared relief gratings with controllable profiles. *J*. *Mater*. *Process*. *Technol*. **317**, 118007.

[52] Wang Z J, Luo X C, Liu H T, Ding F, Chang W L, Yang L, Zhang J G and Cox A. 2021. A high-frequency non-resonant elliptical vibration-assisted cutting device for diamond turning microstructured surfaces. *Int*. *J*. *Adv*. *Manuf*. *Technol*. **112**, 3247-3261.

[53] Zheng Z P, Zhang J F, Feng P F, Li Z W and Wang J J. 2022. Fabrication of hierarchical micro/nanostructures on titanium alloy by combining rotary ultrasonic milling and anodizing. *Manuf*. *Lett*. **34**, 43-48.

[54] Zhang J, Suzuki N and Shamoto E. 2013. Investigation on machining performance of amplitude control sculpturing method in elliptical vibration cutting. *Procedia CIRP* **8**, 328-333.

[55] Kurniawan R and Ko T J. 2014. A new tool holder design with two-dimensional motion for fabricating

micro-dimple and groove patterns. *Int. J. Precis. Eng. Manuf.* **15**, 1165-1171.

[56] Zhang C, Shi G L and Ehmann K F. 2017. Investigation of hybrid micro-texture fabrication in elliptical vibration-assisted cutting. *Int. J. Mach. Tools Manuf.* **120**, 72-84.

[57] Kurniawan R, Ali S, Park K M, Jung S T and Ko T J. 2019. Experimental study of microgroove surface using three-dimensional elliptical vibration texturing. *J. Micro Nano-Manuf.* **7**, 024502.

[58] Wang J J, Yang R, Gao S M, Weng F, Wang Y K, Liao W H and Guo P. 2020. Modulated vibration texturing of hierarchical microchannels with controllable profiles and orientations. *CIRP J. Manuf. Sci. Technol.* **30**, 58-67.

[59] Zheng Z P, Zhang J F, Feng P F and Wang J J. 2023. Controllable fabrication of microstructures on the metallic surface using oblique rotary ultrasonic milling. *Int. J. Mech. Sci.* **237**, 107805.

[60] Song Y, Díaz-Marín C D, Zhang L N, Cha H, Zhao Y J and Wang E N. 2022. Three-tier hierarchical structures for extreme pool boiling heat transfer performance. *Adv. Mater.* **34**, 2200899.

[61] Kim T, Kwon S, Lee J, Lee J S and Kang S. 2022. A metallic anti-biofouling surface with a hierarchical topography containing nanostructures on curved micro-riblets. *Microsyst. Nanoeng.* **8**, 6.

[62] Zhang Y M *et al*. 2022. Cell osteogenic bioactivity mediated precisely by varying scaled micro-pits on ordered micro/nano hierarchical structures of titanium. *Regener. Biomater.* **9**, rbac046.

[63] Merchant M E. 1945. Mechanics of the metal cutting process. I. Orthogonal cutting and a type 2 chip. *J. Appl. Phys.* **16**, 267-275.

[64] Yin S, Wang X F, Xu B P and Li W Y. 2010. Examination on the calculation method for modeling the multi-particle impact process in cold spraying. *J. Therm. Spray Technol.* **19**, 1032-1041.

[65] Grazka M and Janiszewski J. 2012. Identification of johnson-cook equation constants using finite element method. *Eng. Trans.* **60**, 215–223.

[66] Cheng K and Huo D H. 2013. *Micro-cutting: fundamentals and applications*. (John Wiley & Sons, Ltd., Chichester).

[67] Li Z H, Yan Y D, Hu X, Xu C Y, Li Y and Geng Y Q. 2023. Nanomachining of van der Waals nanowires: process and deformation mechanism. *Int. J. Mach. Tools Manuf.* **188**, 104018.

[68] Merchant M E. 1945. Mechanics of the metal cutting process. II. Plasticity conditions in orthogonal cutting. *J. Appl. Phys.* **16**, 318-324.

[69] Yang Y, Xiang J Q and Zhao Z J. 2023. An analytical cutting force model for elliptical vibration texturing of nano-grating surfaces. *J. Mater. Process. Technol.* **315**, 117901.

[70] Lu H, Zhu L D, Yang Z C, Lu H, Yan B L, Hao Y P and Qin S Q. 2021. Research on the generation mechanism and interference of surface texture in ultrasonic vibration assisted milling. *Int. J. Mech. Sci.* **208**, 106681.

[71] Liu X F, Zhang J H, Hu X Y and Wu D B. 2019. Influence of tool material and geometry on micro-textured surface in radial ultrasonic vibration-assisted turning. *Int. J. Mech. Sci.* **152**, 545-557.

[72] Du H H, Yip W, Zhu Z W and To S. 2021. Development of a two-degree-of-freedom vibration generator for fabricating optical microstructure arrays. *Opt. Express* **29**, 25903-25921.

[73] Shen X H, Shi Y L, Zhang J H, Zhang Q J, Tao G C and Bai L J. 2020. Effect of process parameters on micro-textured surface generation in feed direction vibration assisted milling. *Int. J. Mech. Sci.* **167**, 105267.

[74] Börner R, Winkler S, Junge T, Titsch C, Schubert A and Drossel W G. 2018. Generation of functional surfaces by using a simulation tool for surface prediction and micro structuring of cold-working steel with

ultrasonic vibration assisted face milling. *J. Mater. Process. Technol.* **255**, 749-759.

[75] Li Z W, Zhang J F, Zheng Z P, Feng P F, Yu D W and Wang J J. 2023. Vibration chiseling: a backward-moving cutting for the high-efficiency fabrication of short metallic microfibers. *Manuf. Lett.* **36**, 80-85.

[76] Guo X G, Li Y, Cai L Q, Guo J, Kang R K, Jin Z J and Guo D M. 2020. Effects of tool edge radius on chip formation during the micromachining of pure iron. *Int. J. Adv. Manuf. Technol.* **108**, 2121-2130..